Role of thermal disequilibrium on natural convection in porous media: Insights from pore-scale study

Hamid Karani*
School of Earth & Atmospheric Sciences, Georgia Institute of Technology, Atlanta, GA 30332, USA

Christian Huber
Department of Earth, Environmental and Planetary Sciences, Brown University, Providence, RI 02912, USA
(Received 28 December 2016; published 31 March 2017)

The present study investigates the role of thermal nonequilibrium on natural convection in a fluid-saturated porous medium heated from below. We conduct high-resolution direct numerical simulation at the pore scale in a two-dimensional regular porous structure by means of the thermal lattice-Boltzmann method (LBM). We perform a combination of linear stability analysis of continuum-scale heat transfer models, and pore-scale and continuum-scale simulations to study the role of thermal conductivity contrasts among phases on natural convection. The comparison of pore-scale lattice-Boltzmann simulations with linear stability analysis reveals that traditional continuum-scale models fail to capture the correct onset of convection, convection mode, and heat transfer when the thermal conductivity of the solid obstacles does not match that of the fluid.

DOI: 10.1103/PhysRevE.95.033123

I. INTRODUCTION

Modeling convective heat transfer in porous media is generally based on using average-scale formulations for the momentum and energy equations. Darcy and extended Darcy models such as Dupuit-Darcy (sometimes known as Forchheimer's model) and Brinkman-Darcy models are the most commonly used to simulate fluid flow through a porous medium [1]. The formulation of the average-scale energy equation depends on the assumption of local thermal equilibrium among the different phases [1]. Assuming a local thermal equilibrium (LTE) allows us to recast the statement of energy conservation into a single temperature equation, while the absence of local thermal equilibrium, local thermal nonequilibrium (LTNE), requires coupled energy equations, one for each phase. The degree of disequilibrium between phases during natural thermal convection has therefore a significant effect on heat transfer and convective patterns.

In the present study, we consider a fluid-saturated porous medium subjected to a vertical temperature gradient. This problem, which is analogous to Rayleigh-Bénard convection, was first studied by Horton-Rogers [2] and Lapwood [3] (hereafter called HRL convection). They performed a linear stability analysis and identified the condition under which convective patterns emerge. The transition is generally parameterized by a modified critical Rayleigh number which is predicted to be $\mathrm{Ra}_{cr} = 4\pi^2$ for a horizontally infinite porous domain and for a two-dimensional (2D) square box. This critical value is valid as long as the momentum equation follows Darcy' s law and the phases are locally in thermal equilibrium (LTE).

Several experimental studies reported values of heat transfer (Nusselt number) and critical Rayleigh number that deviate from the theoretical predictions made for HRL convection with the Darcy-LTE model, e.g., [4–6]. These experiments also suggest that the contrast in thermal conductivity between the solid and liquid phases exacerbates the discrepancy.

The present study is focused on constraining the role of solid-to-fluid thermal conductivity ratio to test which model for the energy conservation at the continuum scale (LTE versus LTNE) is better suited to study HRL convection in porous media. The knowledge of *pore-scale* temperature distribution in both fluid and solid phases is required for verifying the consistency of the predictions from LTNE models. For this purpose, we conducted direct numerical simulation (DNS) at the pore-scale level over a 2D porous structure consisting of regular arrangements of solid blocks. The advantage of these pore-scale calculations is that they allow us to consider a range of solid-to-fluid thermal conductivity ratios and also, it does not rely on a homogenization model for the energy equation (LTE versus LTNE, for example), where the pore-scale information is filtered out. As a result, these DNS calculations are here designed to test the validity of either continuum-scale model under different conditions. The numerical model is based on the lattice-Boltzmann method (LBM) [7,8], and the momentum and energy equations are solved at the pore scale and do not require closure equations for permeability or effective thermal properties.

We first analyze the performance of LTNE models to assess the role of local thermal disequilibrium on heat transfer around and beyond the critical Rayleigh number Ra_{cr}. We perform linear stability analysis for finding the critical Rayleigh number and also the critical convective mode at the onset of convection as a function of the interphase heat transfer coefficient. We then conduct DNS simulations over a range of Rayleigh numbers for various solid-to-fluid thermal conductivity ratios to find (1) the degree of local thermal disequilibrium under steady conditions, (2) the prevailing convective mode near the onset of convection, (3) the critical Rayleigh number where convection starts, and (4) the relationship between heat transfer (Nusselt number Nu) and thermal forcing as represented by Nu(Ra) curves.

The organization of the paper is as follows: In Sec. II, we present the mathematical formulation of the pore-scale and continuum-scale models for HRL convection. Section III presents the thermal performance of LTNE models. Section IV

*hamid.karani@gatech.edu

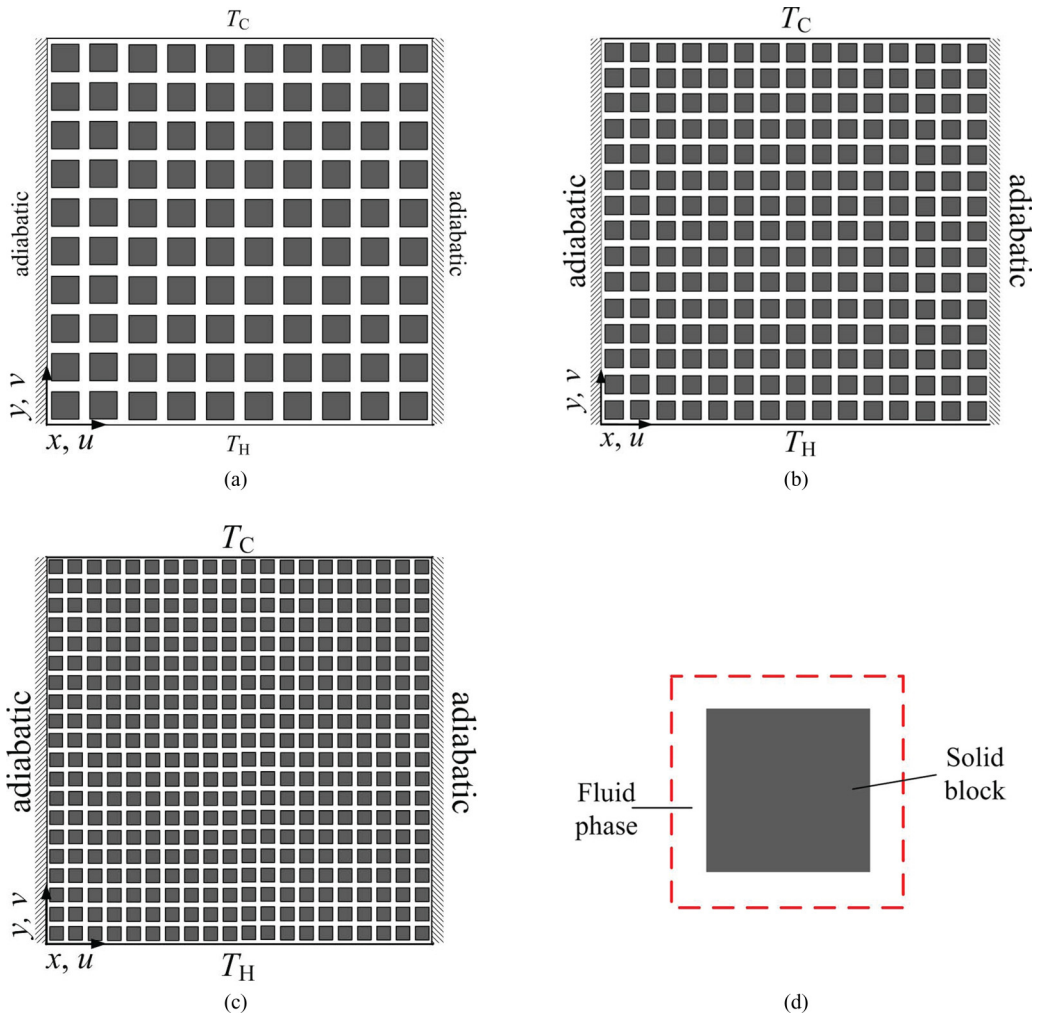

FIG. 1. Physical domains in the pore-scale study: (a) 10×10 unit cells, (b) 15×15 unit cells, (c) 20×20 unit cells, and (d) unit cell (dashed line showing the periodicity).

provides the results of pore-scale DNS calculations for HRL convection and the comparison of the results with the corresponding LTE and LTNE models. Finally, we discuss possible causes for the mismatch between continuum and pore-scale models in Sec. V.

II. Mathematical FORMULATION

A. Pore scale

We consider the 2D porous media shown in Fig. 1 as our pore-scale physical domains. The 2D porous enclosure has the aspect ratio 1, Γ = height (H)/width (W)=1. The domain consists of 10×10, 15×15, and 20×20 regular and identical unit cells containing square solid blocks of dimension d such that H/d ranges from 14.1 to 28.2. In Fig. 1, the solid blocks are represented by the gray pixels, while the white pixels between the blocks represent the fluid phase. The porosity of the medium is $\varphi = 0.5$ for all pore-scale domains. The choice of 20 layers in our study is solely based on the compromise between the computational cost (due to the computationally intensive simulations for detailed pore-scale analyses) and retrieving a statistically relevant set of results to interpret at the continuum scale. Since we intentionally designed our domain to be *a priori* periodic, it becomes natural to select the unit cell to be the representative volume element (RVE) and also the averaging volume [9], and it thus eliminates the uncertainty in defining the representative averaging volume. The same procedure has been used extensively in similar studies (see, for example, Refs. [9–13]). We show later in Sec. V that the pore-scale simulations successfully recover the important physical features of the HRL convection and the results are independent of the coarseness of the solid blocks.

The pore-scale analysis of HRL convection is based on the direct numerical simulation of conservation equations for both constituents for the two-dimensional porous media shown in Fig. 1. For the fluid phase, the Navier-Stokes and energy equations are (using the Boussinesq approximation)

$$\nabla \cdot \boldsymbol{u} = 0, \tag{1}$$

$$\frac{\partial \mathbf{u}}{\partial t} + (\mathbf{u}\cdot\nabla)\mathbf{u} = -\frac{1}{\rho}\nabla P + \nu\nabla^2\mathbf{u} + \mathbf{g}\beta(T - T_{\text{ref}}), \tag{2}$$

$$(\rho c)_f \frac{\partial T}{\partial t} + \nabla\cdot[(\rho c)_f \mathbf{u}T] = \nabla\cdot(k_f\nabla T), \tag{3}$$

where **u** is the pore-scale velocity field, P is the pressure, T is the temperature, ν is the kinematic viscosity of the fluid, β is the thermal expansion coefficient, **g** is the gravitational acceleration, k refers to thermal conductivity, c is the specific heat, and ρ the density of the fluid phase (subscript f). For the solid phase, the energy equation reduces to

$$(\rho c)_s \frac{\partial T}{\partial t} = \nabla \cdot (k_s \nabla T), \tag{4}$$

where the subscript s refers to the properties of the solid phase. Across a fluid-solid interface I, the continuity of temperature and normal heat flux yield

$$T^{I,+} = T^{I,-}$$
$$\mathbf{n} \cdot (k\nabla T + \rho c \mathbf{u} T)^{I,+} = \mathbf{n} \cdot (k\nabla T + \rho c \mathbf{u} T)^{I,-}, \tag{5}$$

where **n** is normal to the interface, and + and − denote the different sides of the interface. The hydrodynamic and thermal boundary conditions are those for HRL convection and are set with

$$(u,v) = 0, \quad T = T_H, \quad \text{for} \quad y = 0, \quad \text{for all} \quad x, \tag{6}$$

$$(u,v) = 0, \quad T = T_C, \quad \text{for} \quad y = H, \quad \text{for all} \quad x, \tag{7}$$

$$(u,v) = 0, \quad \frac{\partial T}{\partial x} = 0, \quad \text{for} \quad x = 0,1, \quad \text{for all} \quad y. \tag{8}$$

These governing equations are solved with the lattice-Boltzmann method [7,8,14]. However, since the fluid-saturated porous matrix at the pore-scale level comprises a thermally heterogeneous system due to different thermophysical properties between solid and fluid, we resort to a thermal LBM model designed to satisfy the conjugate interface boundary conditions described by (5). In recent years, several thermal LBM models have been developed for solving the conjugate heat transfer problems [15–24]; the present calculations follow the procedure described in [15] for the thermal energy equation. We used a single-relaxation time D2Q9 lattice-Boltzmann model for both the velocity and temperature distribution functions. There are several approaches for applying the no-slip boundary condition [25,26]. In the present study, Zou-He's bounce-back scheme of the nonequilibrium part of the particle distribution functions [26] is used to implement no-slip conditions at solid boundaries, and the thermal counterslip method is applied to enforce both Dirichlet and Neumann boundary conditions for the energy equation [27,28]. In the pore-scale simulations, we used 60×60 grid-point resolution over each unit cell. The lattice-Boltzmann parameters were selected such that the Mach number is sufficiently small to stay within the incompressibility limit.

The regular configuration of repeated unit cells provides us with a straightforward test for the LTE and LTNE assumptions. We can compute local phase averages $\langle T_i \rangle^i$ over each unit cell with

$$\langle T_f \rangle^f = \frac{1}{V_f} \int_V T_f \, dV = \frac{1}{\phi V} \int_V T_f \, dV,$$
$$\langle T_s \rangle^s = \frac{1}{V_s} \int_V T_s \, dV = \frac{1}{(1-\phi)V} \int_V T_s \, dV. \tag{9}$$

In order to compare the pore-scale results with the continuum-scale predictions, we need to compute the Darcy-Rayleigh number Ra* and average Nusselt number Nu*, which are defined as

$$\mathrm{Ra}^* = \frac{g\beta(T_H - T_C)KH}{\alpha_m \nu_f} = \mathrm{Ra}_f \mathrm{Da} \frac{k_f}{k_m}$$
$$\mathrm{Ra}_f = \frac{g\beta(T_H - T_C)H^3}{\alpha_f \nu_f}, \quad \mathrm{Da} = \frac{K}{H^2}$$
$$\mathrm{Nu}^* = 1 + \frac{1}{A} \frac{\int_A u_y T \, dA}{\alpha_m \Delta T / H}, \quad \alpha_m = \frac{k_m}{(\rho c)_f}. \tag{10}$$

Ra_f is the conventional Rayleigh number based on the fluid properties. In Ra*, K is the permeability of the porous medium and α_m is the thermal diffusivity based on stagnant thermal conductivity of the solid matrix and the hosted fluid k_m. Da is the Darcy number of the porous medium. We use our LBM model to compute the permeability and average properties of the heterogeneous media from the pore-scale calculations.

B. Continuum scale

Assuming local thermal equilibrium, HRL convection at the continuum scale is described by

$$\nabla \cdot \mathbf{q} = 0, \tag{11}$$

$$\frac{\mu}{K}\mathbf{q} = -\nabla P + \rho \mathbf{g}, \tag{12}$$

$$(\rho c)_m \frac{\partial T}{\partial t} + (\rho c)_f \mathbf{q} \cdot \nabla T = k_m \nabla^2 T, \tag{13}$$

where T is the local temperature averaged over both phases, c is the specific heat, and ρ is the density. K is the permeability of the porous medium, P is the pressure, μ is the dynamic viscosity of the fluid, and **q** is the seepage velocity (Darcy flux). The subscripts m and f refer to the properties of the solid or fluid mixture and the fluid, respectively. Equations (12) and (13) are coupled through the Boussinesq approximation. It should be mentioned that k_m is not only a function of the thermal conductivity of each phase, but it depends strongly on the structure of the porous medium. This structural control has been studied extensively, both theoretically and experimentally, and it is found that k_m cannot be defined simply as the volumetric arithmetic or harmonic mean of the fluid and solid thermal conductivities [29,30].

We can relax the local thermal equilibrium assumption by developing a model where the energy conservation for each phase is considered separately and coupled through an interphase heat exchange term [1]. This allows the two phases to experience different temperatures locally, which may appear more consistent with convection in porous media where the fluid and solid thermophysical properties are different and the advection of heat may be highly spatially heterogeneous [1]. There are multiple derivations for the two-temperature models, and the reader is referred to Rees and Pop for an overview of the recent developments with LTNE approaches [31]. In the present study, we consider two common models, which are referred to as LTNE-1 and LTNE-2. The difference between the two models stems from the way they were developed. The LTNE-1 model, which is the simplest two-temperature model,

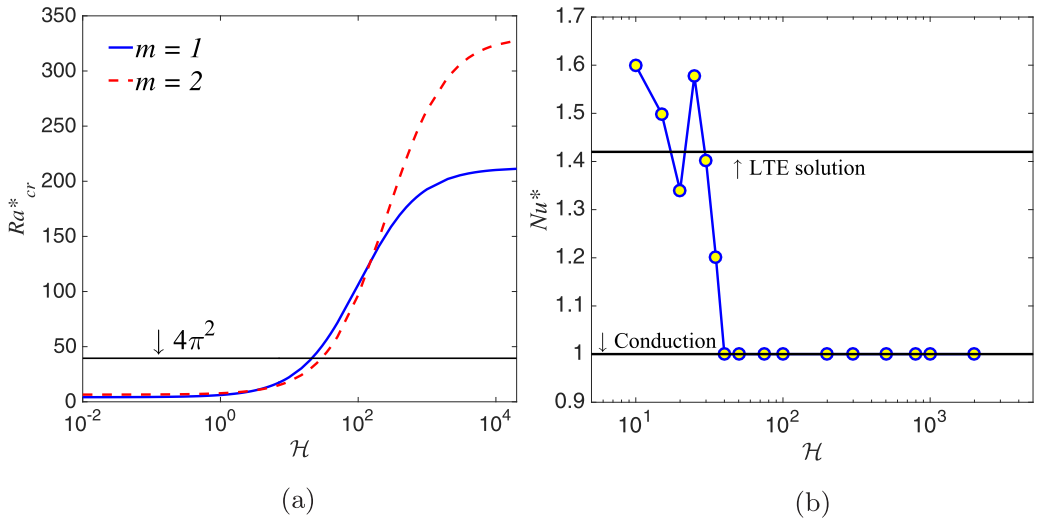

FIG. 2. LTNE-1: (a) Variation of critical Rayleigh number Ra_{cr} for the horizontal wave modes $m = 1$ and 2 with dimensionless interphase heat transfer coefficient $\mathcal{H}$; (b) variation of Nusselt number Nu with $\mathcal{H}$ for $\mathrm{Ra} = 50$.

is based on the following set of equations [1,31]:

$$\varphi(\rho c)_f \frac{\partial T_f}{\partial t} + (\rho c)_f \mathbf{q}\cdot\nabla T_f = \varphi k_f \nabla^2 T_f + h(T_s - T_f), \tag{14}$$

$$(1-\varphi)(\rho c)_s \frac{\partial T_s}{\partial t} = (1-\varphi)k_s \nabla^2 T_s - h(T_s - T_f), \tag{15}$$

where h is the interphase heat transfer coefficient responsible for the nonequilibrium heat transfer between the different phases and φ is the porosity of the medium. The subscript s and f refer to solid and fluid phase properties, respectively. Summing Eqs. (14) and (15) and assuming thermal equilibrium reduces the model to the single temperature (LTE) model with an effective mixture thermal conductivity $k_m = \varphi k_f + (1-\varphi)k_s$, which is a volumetric average and not a true stagnant conductivity. This is one of the inconsistencies of the LTNE-1 model in the LTE limit. On the other hand, if we apply volume averaging over the microscale energy equation, extra coupling terms between solid and fluid phases appear which are ignored in this (LTNE-1) formulation. Even for the case of pure heat diffusion, it has been shown that these extra coupling terms cannot be omitted from the general energy equation [10]. Keeping this in mind, Nakayama *et al.* [32] used the volume-averaging process and extended the previous works for heat conduction [10,33] to convection-conduction heat transfer and derived the following LTNE-2 equations:

$$\begin{aligned}\varphi(\rho c)_f \frac{\partial T_f}{\partial t} + (\rho c)_f \mathbf{q}\cdot\nabla T_f &= \nabla\cdot[(\varphi k_f + k_f G + k_{\mathrm{dis}})\nabla T_f] \\ &\quad + (-k_s G)\nabla^2 T_s + h(T_s - T_f),\end{aligned} \tag{16}$$

$$\begin{aligned}(1-\varphi)(\rho c)_s \frac{\partial T_s}{\partial t} &= \nabla\cdot\{[(1-\varphi)k_s + k_f G\kappa]\nabla T_s\} \\ &\quad + (-k_s G)\nabla^2 T_f - h(T_s - T_f),\end{aligned} \tag{17}$$

where k_{dis} is the thermal dispersion conductivity, and $\kappa = k_s/k_f$ and G is the tortuosity parameter [33]. The following equation has been proposed for calculating the tortuosity parameter G [33]:

$$G = \frac{k_m/k_f - \varphi - (1-\varphi)\kappa}{(\kappa-1)^2}, \tag{18}$$

which always gives a negative value for G and recovers the true stagnant thermal conductivity of the medium k_m. This can be easily verified by summing up Eqs. (16) and (17) together and assuming local thermal equilibrium, which yields $k_m = \varphi k_f + (1-\varphi)k_s + k_f(1-\kappa)^2 G$. Therefore, by knowing the thermophysical properties of each phase and also the stagnant thermal conductivity of the medium, we can find the value of the tortuosity parameter.

A critical aspect of using both LTNE formulations lies in the determination of the appropriate value of h. In general, h is known to depend on many factors, including the detailed geometry of the porous medium, the porosity, the phase conductivities and diffusivities, and also the pore-scale velocity field [34,35].

III. LTNE RESULTS

We perform a linear stability analysis for both LTNE models (details are provided in the Appendix) to find the critical mode and the critical Rayleigh number at the onset of convection. Figure 2 presents the results for the LTNE-1 model. Panel (a) shows how the critical Rayleigh number Ra_{cr} of the horizontal wave modes $m = 1$ and 2 changes with the dimensionless interphase heat transfer coefficient $\mathcal{H}$ [defined in the Appendix, Eq. (A9)]. The critical Rayleigh number at the onset of convection for each $\mathcal{H}$ is the minimum of the corresponding values for the two modes ($m = 1$, 2; higher modes yield even greater Ra_{cr}, not shown here). HRL convection is a multistable thermal system, meaning that different convection modes may coexist at a given Rayleigh number. One of the distinguishing features of convective patterns with different horizontal modem is the amount of

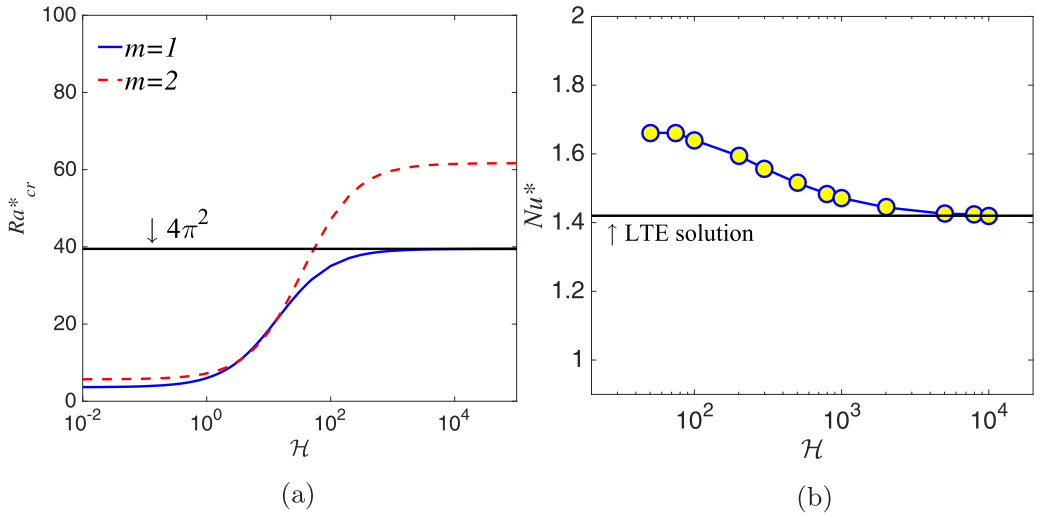

FIG. 3. LTNE-2: (a) Variation of critical Rayleigh number Ra_{cr} for the horizontal wave modes $m = 1$ and 2 with dimensionless interphase heat transfer coefficient $\mathcal{H}$; (b) variation of Nusselt number Nu with $\mathcal{H}$ for $\mathrm{Ra} = 50$.

heat that is transferred through the domain. Therefore, it is crucial that continuum-scale formulations, such as LTNE-1 and LTNE-2 models, predict a consistent and correct mode.

Figure 2(a) shows that for the LTNE-1 model, in the limit $\mathcal{H} \to \infty$, i.e., local thermal equilibrium between solid and fluid phases, the single-cell convection mode $m = 1$ is selected at the onset of convection and Ra_{cr} is higher than $4\pi^2$, the critical Rayleigh number based on the Darcy-LTE model for a horizontally infinite domain or a square box (aspect ratio 1). The inconsistency here results from the mixture effective thermal conductivity k_m to differ from the true stagnant thermal conductivity of the medium in the LTNE-1 model. On the other hand, as $\mathcal{H} \to 0$, i.e., extreme local thermal disequilibrium between solid and fluid phases, Ra_{cr} is lower than $4\pi^2$, indicating that convection initiates at lower Ra than predicted by the LTE model. In both limiting cases of $\mathcal{H} \to 0$ and ∞, $m = 1$ is the critical mode at the onset of convection. However, for intermediate values of $\mathcal{H}$, Fig. 2 shows that the second horizontal mode $m = 2$ becomes the favored mode. This explains the local peak in $\mathrm{Nu}(\mathcal{H})$ for a fixed Ra (here 50), shown in Fig. 2(b). At high values of $\mathcal{H}$, since Ra_{cr} is larger than 50, convection is absent and the Nusselt number is equal to 1, as expected.

The behavior of the LTNE-2 model is different from LTNE-1, as shown in Fig. 3. Panel (a) shows the dependence of Ra_{cr} on $\mathcal{H}$. First for the whole range of $\mathcal{H}$ values, the dominant horizontal mode at the onset of convection is $m = 1$. Second, we can observe that, in contrast with LTNE-1, the critical Rayleigh number recovers the correct value in the LTE regime ($\mathcal{H} \to \infty$). On the other hand, we find Ra_{cr} to be always smaller than $4\pi^2$ over the whole range of interphase heat transfer coefficient and decreases with the degree of disequilibrium between phases. This suggests that, under local thermal disequilibrium conditions, the onset of convection is expected to occur at lower Ra with model LTNE-2 than LTE would predict, which also affects the Nusselt number (higher than expected from LTE model), as observed in Fig. 3(b).

IV. PORE-SCALE RESULTS

A. Degree of local thermal disequilibrium

Figures 4 and 5 illustrate, respectively, the pore-scale temperature and velocity maps of 20×20 unit cells for different ratios of solid-to-fluid thermal conductivities $\kappa = k_s/k_f$ at $\mathrm{Ra}^* = 80$. The detailed temperature and velocity maps in the pore-scale simulations of Figs. 4 and 5 enable us to image and study small- (pore-) scale flow and temperature distributions and test several average-scale assumptions, including local thermal equilibrium and non-Darcian effects. We use Eq. (9) and calculate the phase-averaged temperatures $\langle T_f \rangle^f$ and $\langle T_s \rangle^s$ over each unit cell [shown in Fig. 1(d)] in the pore-scale temperature solution in Fig. 4. This allows us to quantify the degree of local thermal disequilibrium between phase-averaged temperatures for each unit cell.

Figure 6 shows the maximum disequilibrium between phase-averaged temperatures observed at each Rayleigh number and for different thermal conductivity ratios. The maximum observed disequilibrium is below 2% for all κ values.

In order to quantify the significance of this level of thermal disequilibrium, we use the pore-scale data for the case where the solid matrix and fluid have the same thermal conductivity, i.e., $\kappa = 1$. Since $\kappa = 1$, the stagnant thermal conductivity of the porous medium is equal to the thermal conductivities of solid or fluid, i.e., $k_m = k_s = k_f$. In other words, the unit cell is thermally homogeneous at the pore-scale level. We can use this case for comparing the pore-scale data with the corresponding Darcy-LTE solution to verify whether a thermal disequilibrium of $\lesssim 2\%$ leads to departure from LTE assumption or not. For comparison with the average-scale solution, the Darcy number of the porous structures in Fig. 4 is calculated from our LBM model and is found to be $\mathrm{Da} = 2.435\times10^{-5}$, $\mathrm{Da} = 1.195\times10^{-5}$, and $\mathrm{Da} = 7.594\times10^{-6}$ for 10×10, 15×15, and 20×20 domains, respectively. Figure 7 shows the comparison of the pore-scale heat transfer data with those from the average-scale formulations of [36] for a square box. The average-scale solution of Henry *et al.* [36] is

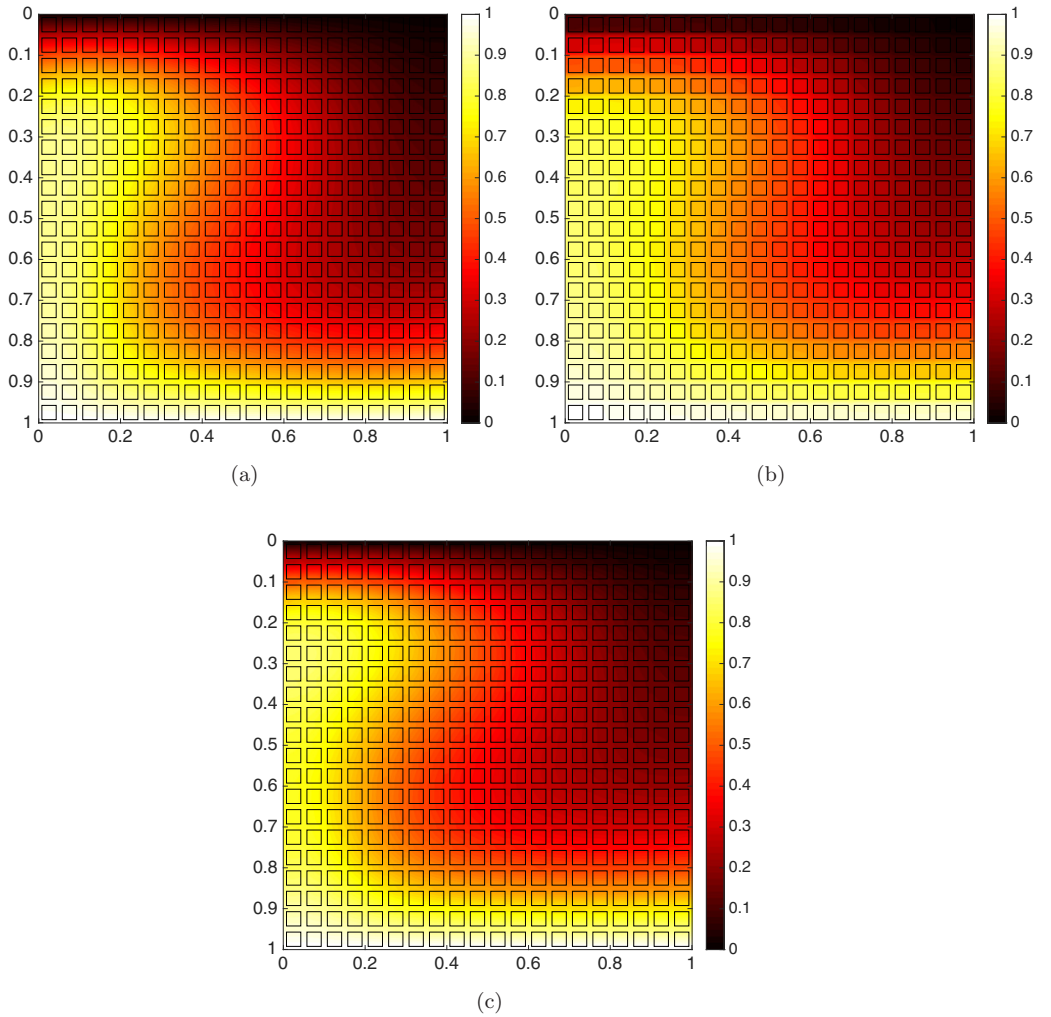

FIG. 4. Steady temperature maps at $\mathrm{Ra}^* = 80$ for 20×20 of unit cells: (a) $\kappa = 1$, (b) $\kappa = 50$, and (c) $1/13$.

based on a Darcian description of the momentum conservation with a single-temperature energy equation, i.e., Eqs. (12) and (13). There is an excellent agreement between the pore-scale data for $\kappa = 1$ and the continuum-scale solution of Henry *et al.* [36]. The current pore-scale results for the case of $\kappa = 1$ show that the onset of convection agrees with the theoretical value of $\mathrm{Ra}^* = 4\pi^2$ and that the average heat transfer behavior after the onset of convection follows the one predicted by the classical Darcy-LTE formulations. This justifies that the local thermal disequilibrium of $\lesssim 2\%$ observed at the pore scale is not significant and a single-energy model at the average scale provides accurate description of the thermal behavior.

The excellent agreement between the pore-scale data and the LTE-Darcy solution in Fig. 7 further confirms that the calculated permeability of the medium by using LBM is accurate and that non-Darcian effects are negligible for the present porous configuration (small Darcy number). The calculated pore-scale Reynolds number is also smaller than 1, further confirming that our simulations satisfy the Darcian regime.

B. Nu^*– Ra^* scaling when $\kappa \neq 1$

We now turn our attention to the effect of thermal conductivity contrasts between the solid and fluid on the average heat flux in the domain. Figure 8 summarizes the results for the average Nusselt number for $\kappa = 50$ and $\kappa = 1/13$ over a range of Ra around the onset of convection for the case of 20×20 unit cells. Recalling that $\kappa = k_s/k_f$, the data on Fig. 8 shows that when solid is more conductive than the fluid, for example, in $\kappa = 50$, the average Nusselt number falls below the results for $\kappa = 1$, the values predicted by Darcy-LTE solutions. The opposite trend is observed when the fluid is more conductive than the solid, i.e., $\kappa = 1/13$. This discrepancy between LTE $\mathrm{Nu}^* - \mathrm{Ra}^*$ results and our pore-scale calculations is not caused by local thermal disequilibrium between phases, as the latter is found to be small and comparable to what we observed for simulations with $\kappa = 1$, which matched accurately with the LTE predictions. If we set $\mathcal{H}$ in both LTNE models to a value corresponding to about 2%–3% of thermal disequilibrium between the fluid and solid phases, we find that both LTNE models are not able to match the observed heat transfer (Nu^*) found in the pore-scale simulations (Fig. 8).

Comparing the pore-scale data in Fig. 8 with those from κ=1 displayed in Fig. 7 shows that, not only does the $\mathrm{Nu}^*(\mathrm{Ra}^*)$ scaling for $\kappa \neq 1$ deviate from the LTE solution, but also the onset of convection departs from the classical value of $\mathrm{Ra}^*=4\pi^2$. We define the critical Rayleigh number as the point

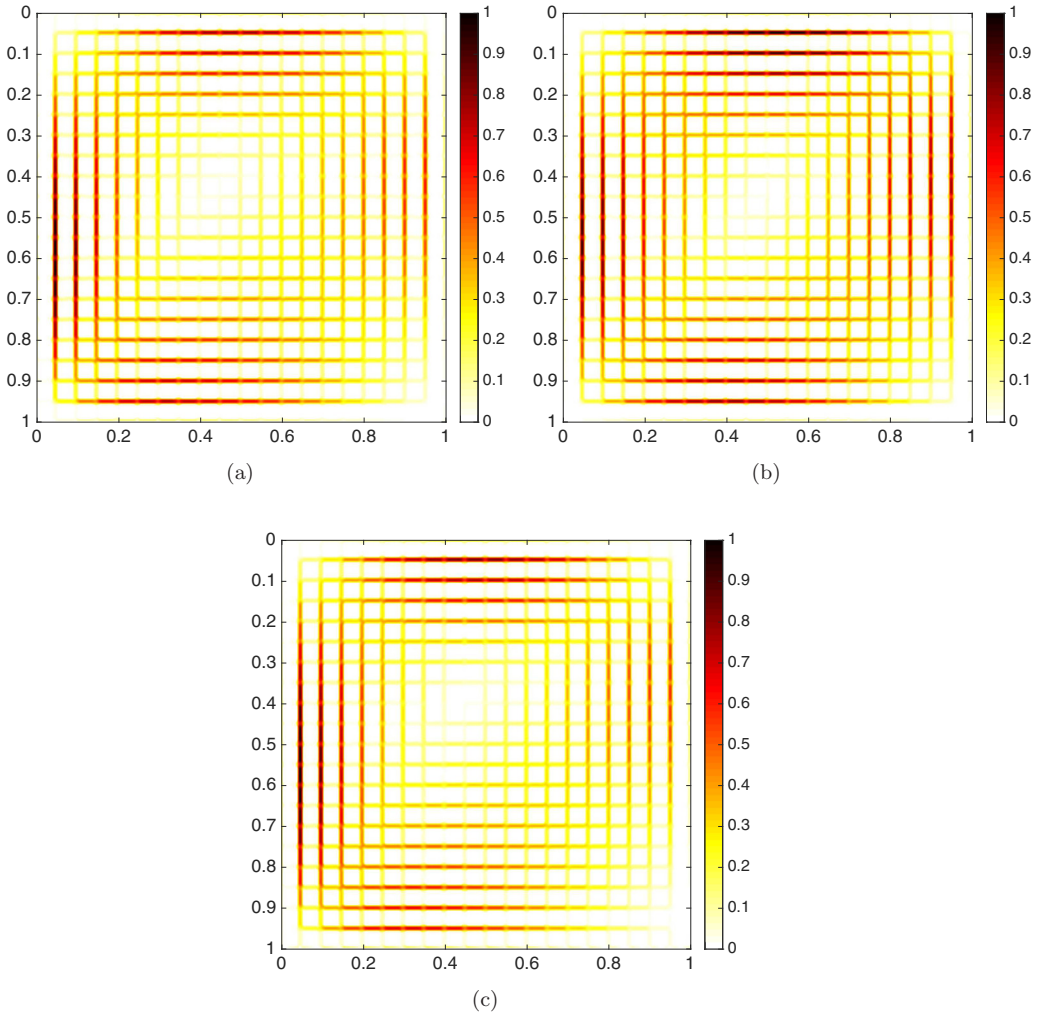

FIG. 5. Steady velocity magnitude maps at $\mathrm{Ra}^* = 80$ for 20×20 of unit cells: (a) $\kappa = 1$, (b) $\kappa = 50$, and (c) $1/13$.

where a sudden change in the slope of the $\mathrm{Nu}^* - \mathrm{Ra}^*$ curve occurs. When the solid and fluid have similar thermal conductivities, a critical point defines the Rayleigh number value above which $\mathrm{Nu}^* > 1$. However, when the thermal properties of the solid and fluid are different, Nu^* is not necessarily equal to 1 below Ra^*_{cr} because small-scale fluid motion around each cell can slightly perturb the heat transfer (uncritical convection). For $\kappa = 1/13$, convection initiates well before $4\pi^2$, while it is shifted to slightly higher values than $4\pi^2$ for $\kappa = 50$. Our pore-scale simulations show that the critical Rayleigh numbers for $\kappa = 1/13$ and 50 are $\mathrm{Ra}^*_{cr} \simeq 35$ and 42, respectively.

Although we argued that we do not expect this discrepancy to arise because of a lack of local thermal equilibrium between phases, it is worthwhile to contrast our pore-scale results with LTNE models and test whether any of the two LTNE models presented here can reconcile the spread in $\mathrm{Nu}^*(\mathrm{Ra}^*)$ and the shift in Ra^*_{cr} observed. According to Fig. 2, explaining the early initiation of convection for $\kappa = 1/13$ ($\mathrm{Ra}^*_{cr} \simeq 35$) based on the LTNE-1 model first would require a significant degree of thermal disequilibrium, and second would predict that the critical horizontal mode just at the onset of convection is $m = 2$. These two outcomes from the LTNE-1 model disagree with our pore-scale results.

Similar issues arise when trying to explain the pore-scale simulation results with the LTNE-2 model. According to Fig. 3(a), if we select an $\mathcal{H}$ value which provides a critical Rayleigh number of around 35 (similar to pore-scale observations for $\kappa = 1/13$), then the numerical solution of the LTNE-2 model predicts a significant local thermal disequilibrium and would also yield Nusselt number values in excess of the LTE ($\kappa = 1$) model. In summary, neither LTNE-1 and LTNE-2 models can explain the shift in the onset of convection and the Nu*(Ra*) dependence self-consistently.

In the absence of a consistent description of the pore-scale results with LTE and LTNE models, the discussions in the next section try to provide an interpretation in terms of a thermal dispersion phenomena in HRL convection which arises from the contrast in thermal conductivity between different phases.

V. DISCUSSION AND CONCLUSION

A. Effect of coarseness

When convection initiates, boundary layers build up at the top and bottom boundaries. As the Rayleigh number increases, these boundary layers shrink in size, resulting in larger temperature gradients and heat flux next to the top

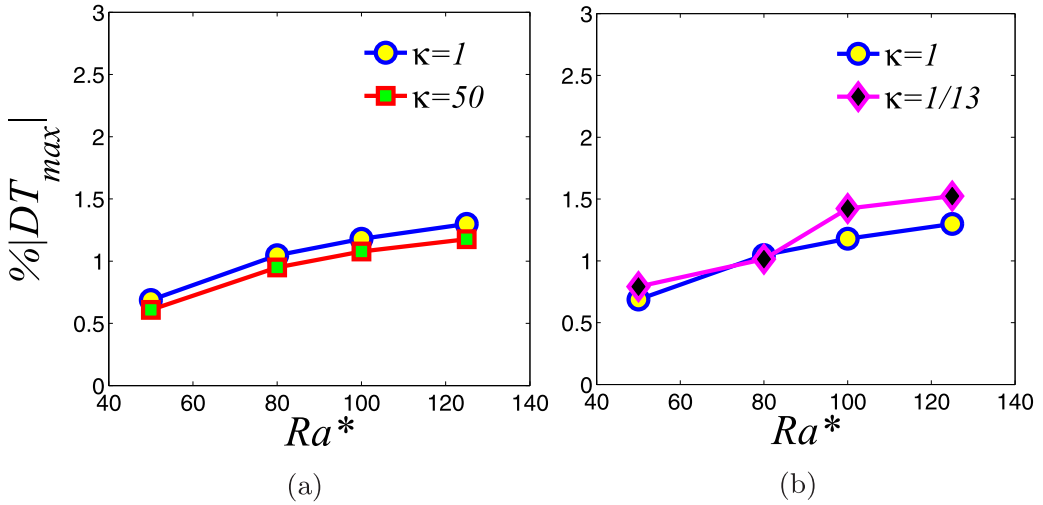

FIG. 6. Percentage of the maximum amount of thermal disequilibrium in the DNS results for the 20×20 of unit cells: (a) $\kappa = 1$ and 50 and (b) $\kappa = 1$ and $1/13$.

and bottom boundaries. Using the continuum-scale equations for modeling HRL convection is valid as long as the pore size of the medium is smaller than any length scale of the flow, especially thermal boundary-layer thickness in HRL convection [37]. Therefore, it is crucial to verify whether the coarseness of the domain in our pore-scale simulation allows us to retrieve average solutions in the continuum limit and resolves the boundary layers accurately.

Figure 9 illustrates the horizontally averaged temperatures in the pore-scale temperature fields of various coarseness using arrays with 10×10, 15×15, and 20×20 solid blocks (Fig. 1). We observe that as the Rayleigh number increases, the boundary layer becomes more localized, thus resulting in higher Nusselt numbers. It also shows that using a coarser number of solid blocks in the 10×10 and 15×15 cases results in similar horizontally averaged temperature profiles to the 20×20 case. Therefore, different numbers of solid blocks offer a similar average thermal behavior, which is further illustrated in the Nu*(Ra*) curves of Fig. 10.

The data in Figs. 9 and 10 show that the observed shift in the onset of convection and the Nu*(Ra*) scalings for different κ and Ra* values are robust over the range of coarseness studied here, which suggests that the resolution and coarseness used are suitable to compare DNS results with continuum model predictions. Figure 11 shows that, for $\kappa = 1$ and $\mathrm{Ra}^* = 100$ in the 20×20 case, the thickness of the boundary layer is at least 4 times larger than the size of the unit cell, which is the true averaging volume for the regular configuration of solid blocks in the pore-scale domain. For Rayleigh numbers larger than the values studied here, however, finer configurations of solid blocks would be required.

B. Thermal dispersion

The deviations between the pore-scale observations and Darcy-LTE predictions can originate from three factors: LTNE effects, non-Darcian effects, and thermal dispersion effects. In the previous sections, we showed that the first two factors are

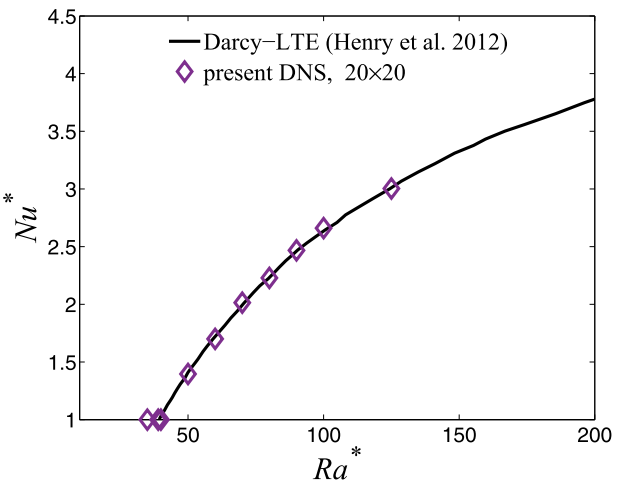

FIG. 7. Nusselt number Nu^* versus Rayleigh number Ra^* for 20×20 of unit cells, $\kappa = 1$.

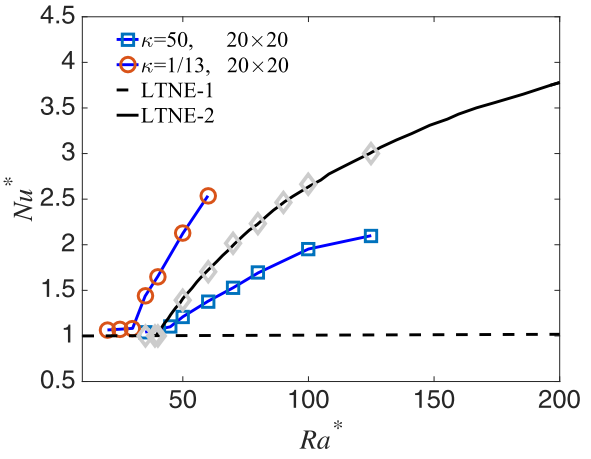

FIG. 8. Nusselt number Nu^* versus Rayleigh number Ra^* for 20×20 unit cells, $\kappa = 50$ and $1/13$. For comparison, the results for the LTE and LTNE models and $\kappa = 1$ are shown, respectively, in gray symbols and black lines.

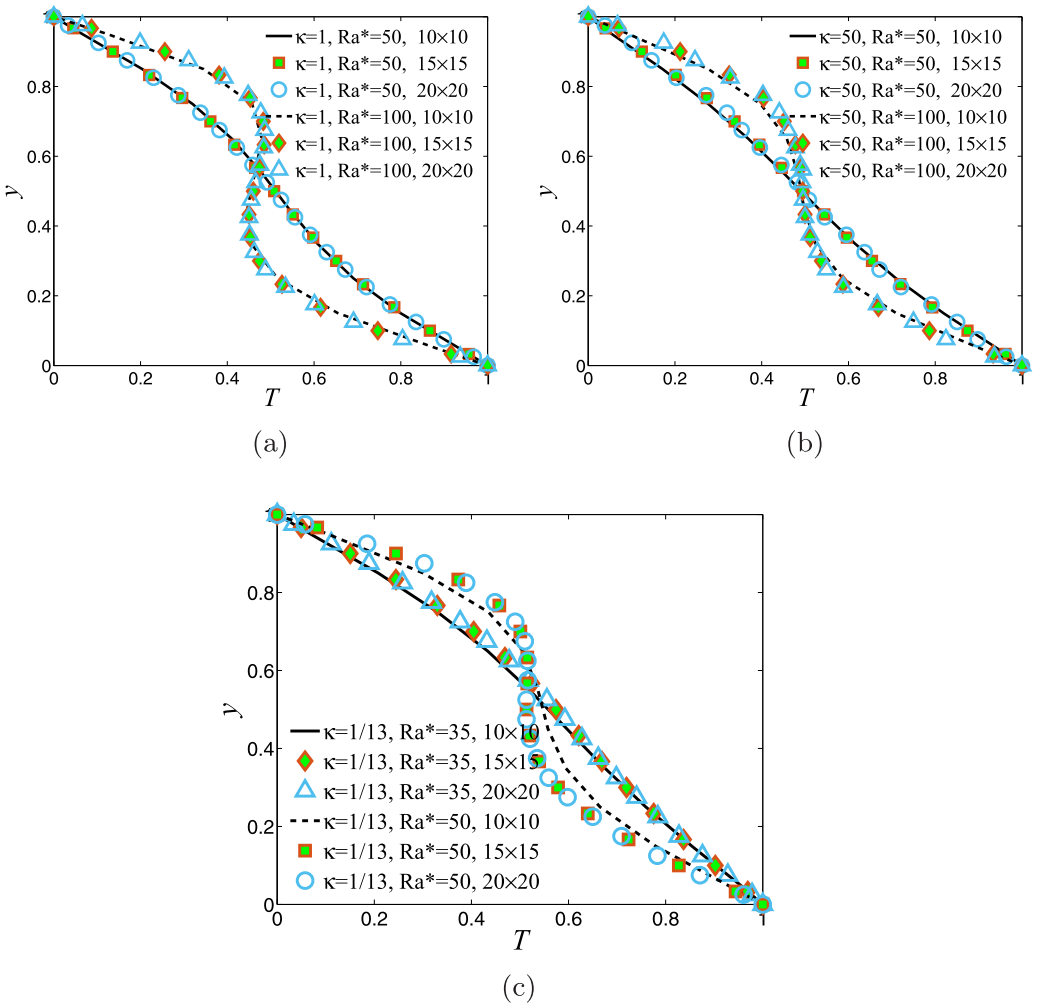

FIG. 9. Horizontally averaged temperatures for 20×20 unit cells: (a) $\kappa = 1$, (b) $\kappa = 50$, and (c) $\kappa = 1/13$.

negligible for the range of κ and Ra* numbers investigated in the pore-scale study. In the present section, we try to investigate the role of thermal dispersion on the observed shift in the onset of convection and the Nu*(Ra*) scalings.

In applying the volume-averaging approach for developing the continuum-scale energy equation (LTE or LTNE models) from the exact pore-scale energy equations, the thermal dispersion term $\nabla \cdot (-(\rho c)_f \langle T' u'_f \rangle^f)$ appears, where T' and u'_f are local temperature and velocity fluctuation fields. (For the detailed derivations, the reader is referred to Refs. [38,39], for example.) For continuum-scale energy equations such as the LTE and LTNE models to be applicable, we need to provide a closure model for the resulting thermal dispersion contribution.

Thermal dispersion is historically modeled as a pseudodiffusive term [40–42], i.e., $\nabla \cdot [-(\rho c)_f \langle T' u'_f \rangle^f] = \nabla \cdot (k_{\text{disp}} \nabla \langle T_f \rangle^f)$, or equivalently,

$$-(\rho c)_f \langle T' u'_f \rangle^f = k_{\text{disp}} \nabla \langle T_f \rangle^f, \tag{19}$$

where k_{disp} is the dispersion conductivity of the porous medium.

Several studies provided models for k_{disp} in porous media based on the theoretical derivations [40–43] and numerical simulations over a periodic single unit cell [44–46]. The available models for the dispersion conductivity can be represented by $k_{\text{disp}} = C \cdot q^n$, where C is a constant, n is some exponent, and q is the local Darcy velocity [or equivalently, as $k_{\text{disp}} = f(\text{Pe or Re})$, where Pe and Re are the pore-scale Péclet and Reynolds number based on the local average velocity of the fluid].

The inherent pseudodiffusive assumption for the thermal dispersion term and its dependence on the local average velocity bears important implications in HRL convection. First, thermal dispersion becomes a nonlinear term in the continuum-scale energy models; therefore it cannot influence the onset of convection [47–49]. Second, previous studies [48,50] showed that the inclusion of thermal dispersion lowers the heat transport for lower values of Ra* but increases Nu* as Ra* is increased. In summary, the available closure models for k_{disp} cannot explain the shift in the onset of convection and the consistently lower or higher Nu*(Ra*) scalings when the solid is more or less conductive than the fluid phase.

There are several experimental evidences for HRL convection that qualitatively support the present pore-scale results. Cheng [4] and Kladias and Prasad [6] reported that for a porous system with the solid matrix being more conductive than the fluid phase, the measured Nusselt numbers are lower than the one predicted by Darcy-LTE and non-Darcy-LTE models.

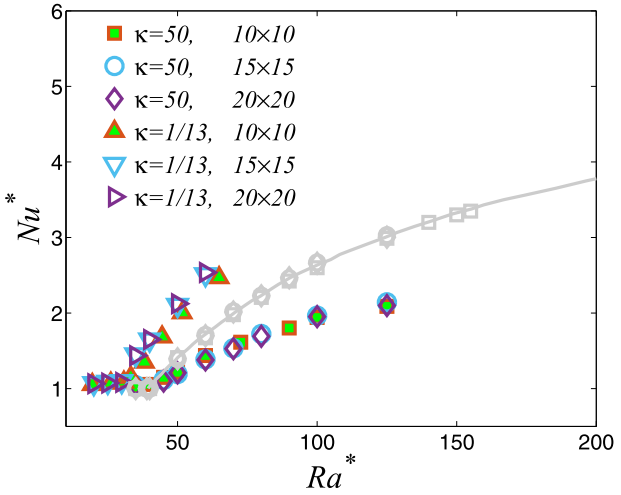

FIG. 10. Effect of coarseness on Nu^{*-} Ra^* scalings. The results for the LTE model and $\kappa = 1$ are shown in gray.

Kladias and Prasad [6] further showed that the inclusion of a thermal dispersion term does not resolve the issue of a lower heat transfer than the LTE case for larger thermal conductivity ratios. The same authors then propose that local thermal disequilibrium may be the cause for the observed deviations between experimental data and theoretical predictions. Lister [49] also observed an early initiation of convection at $Ra^* = 33$ in the HRL convection when the fluid is more conductive than the solid phase, although the author manually shifted the experimental data to start the convection at $4\pi^2$.

The present pore-scale study provides significant insights into the nature of thermal disequilibrium and dispersion in HRL convection. The detailed pore-scale temperature fields reveals that, on one hand, deviations from the predicted critical Rayleigh number and amount of heat transfer can occur even in the presence of local thermal equilibrium. On the other hand, we posit that a nontraditional thermal dispersion effect is responsible for the discrepancy between pore-scale and continuum models. According to the pore-scale observations, $\nabla \cdot (-(\rho c)_f \langle T' u'_f \rangle^f)$ is directly linked to the contrast in thermal conductivities between the solid and fluid phases, and its contribution disappears when both phases share the same thermal conductivity. Also, the present results prompt a reassessment of the pseudodiffusive model of thermal dispersion in the HRL convection. This latter point relaxes the resulting nonlinear nature of the thermal dispersion, which subsequently explains the shift in the onset of convection when solid and fluid phases have different conductivities. Further analysis along this direction is left for a future study.

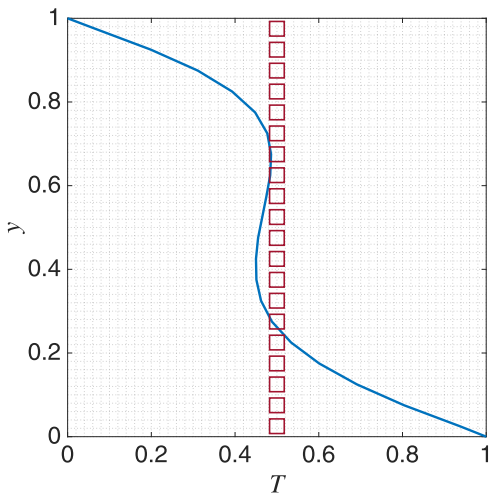

FIG. 11. Horizontally averaged temperature field vs the height of the domain; 20×20 unit cells, $\kappa = 1$, $Ra^* = 100$.

APPENDIX: LINEAR STABILITY ANALYSIS OF LTNE MODELS

In this section, we provide a comprehensive linear stability analysis of LTNE-1 and LTNE-2 models. Banu and Rees [51] were the first to investigate the effect of local thermal disequilibrium on the onset of convection with the LTNE-1 model [Eqs. (14) and (15)]. They showed that for finite values of h, the onset of convection deviates significantly from the classical value of $4\pi^2$. As $h \to \infty$, LTNE recovers LTE and satisfies the classical value $4\pi^2$. However, the definition of the critical Rayleigh number used in their study [Eq. (11) and Fig. 3 in Banu and Rees [51]] is based on a volumetric average for the effective thermal conductivity $k_{m,\max} = \varphi k_f + (1-\varphi)k_s$. As discussed earlier, the stagnant thermal conductivity is generally significantly lower than this value. The original derivation of the critical Rayleigh number $4\pi^2$ is based on the true stagnant thermal conductivity of the medium, and so is the common Nu^{*-} Ra^* correlation. For these reasons, we decided to conduct the linear stability analysis on model LTNE-2 [Eqs. (16) and (17)], and we will find that the LTNE-1 model corresponds to a special case of that more general analysis. In order to have a consistent set of formulations for the stability analysis, we rewrite the LTNE-1 and LTNE-2 models in the following general form (assuming that $k_{\rm dis}$ at the onset of convection can be considered uniform):

$$\varphi(\rho c)_f \frac{\partial T_f}{\partial t} + (\rho c)_f \mathbf{q} \cdot \nabla T_f = k_{ff} \nabla^2 T_f + k_{fs} \nabla^2 T_s + h(T_s - T_f), \qquad \text{(A1)}$$

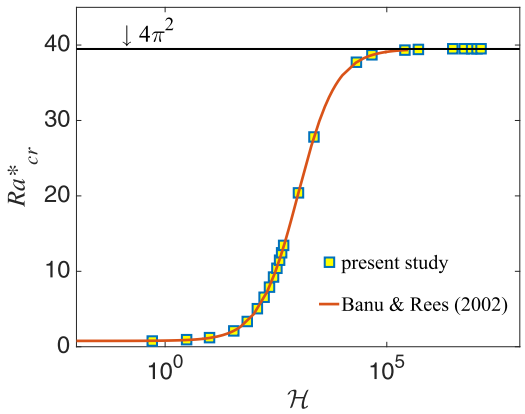

FIG. 12. Recovering the results of Banu and Rees [51] for $k_m = \varphi k_f + (1-\varphi)k_s$ in LTNE-1 model.

$$(1-\varphi)(\rho c)_s \frac{\partial T_s}{\partial t} = k_{ss}\nabla^2 T_s + k_{sf}\nabla^2 T_f - h(T_s - T_f). \tag{A2}$$

For the LTNE-1 model, the thermal conductivities are defined as

$$k_{ff} = \varphi k_f, \quad k_{fs} = k_{sf} = 0,$$
$$k_{ss} = (1-\varphi)k_s, \tag{A3}$$

while for the LTNE-2 model, they are defined as

$$k_{ff} = \varphi k_f + Gk_f + k_{\text{dis}}, \quad k_{fs} = k_{sf} = -Gk_s,$$
$$k_{ss} = (1-\varphi)k_s + Gk_s\kappa. \tag{A4}$$

We define the following dimensionless variables:

$$t^* = t\frac{\alpha_m}{H^2\varphi}, \quad (u,v)^* = (q_x,q_y)^*\frac{H}{\alpha_m},$$
$$(x,y)^* = (x,y)\frac{1}{H},$$
$$\theta_s = \frac{T_s - T_c}{T_h - T_c}, \quad \theta_f = \frac{T_f - T_c}{T_h - T_c}. \tag{A5}$$

We can recast Eqs. (12), (A1), and (A2) with the stream function ψ and normalize lengths, velocity, time, and temperature based on the dimensionless variables in Eq. (A5) to retrieve the following dimensionless governing equations:

$$\nabla^2\psi = \text{Ra}^*\frac{\partial\theta_f}{\partial x}, \tag{A6}$$

$$\frac{\partial\theta_f}{\partial t} + \mathbf{V}\cdot\nabla\theta_f = \gamma\nabla^2\theta_f + \sigma\nabla^2\theta_s + \mathcal{H}(\theta_s - \theta_f), \tag{A7}$$

$$\frac{\partial\theta_s}{\partial t} = \eta\lambda\nabla^2\theta_s + \sigma\lambda\nabla^2\theta_s - \mathcal{H}(\theta_s - \theta_f), \tag{A8}$$

where

$$\gamma = \frac{k_{ff}}{k_m}, \quad \eta = \frac{k_{ss}}{k_m}, \quad \sigma = \frac{k_{sf}}{k_m} = \frac{k_{fs}}{k_m},$$
$$\mathcal{H} = \frac{Hh^2}{k_m}, \quad \lambda = \frac{\varphi}{1-\varphi}\frac{(\rho c)_f}{(\rho c)_s},$$
$$\mathbf{V} = (u,v) = \left(-\frac{\partial\psi}{\partial y}, \frac{\partial\psi}{\partial x}\right), \tag{A9}$$

and Ra* is defined as

$$\text{Ra}^* = \frac{\rho g\beta\boldsymbol{\Delta}TKH}{\nu_f\alpha_m}, \tag{A10}$$

which is now based on true α_m, as opposed to the modified Rayleigh number based on $k_{m,\max} = \varphi k_f + (1-\varphi)k_s$. We follow the same procedure as Banu and Rees [51] for the linear stability analysis. The basic solution (conductive state) has the following form:

$$\psi = 0, \quad \theta_f = \theta_s = 1 - y, \tag{A11}$$

which is perturbed and becomes

$$\psi = \Psi, \quad \theta_f = 1 - y + \Theta_f, \quad \theta_s = 1 - y + \Theta_s. \tag{A12}$$

Inserting this expression into Eqs. (A6)–(A8) and linearizing the nonlinear advective terms gives the following set of linearized equations:

$$\nabla^2\Psi = \text{Ra}^*\cdot\frac{\partial\Theta_f}{\partial x}, \tag{A13}$$

$$\frac{\partial\Theta_f}{\partial t} = \gamma\nabla^2\Theta_f + \sigma\nabla^2\Theta_s - \frac{\partial\Psi}{\partial x} + \mathcal{H}(\Theta_s - \Theta_f), \tag{A14}$$

$$\frac{\partial\Theta_s}{\partial t} = \eta\lambda\nabla^2\Theta_s + \sigma\lambda\nabla^2\Theta_s - \mathcal{H}(\Theta_s - \Theta_f). \tag{A15}$$

We can assume the following solution form for the velocity and temperature fields:

$$\Psi = A_1 \sin n\pi y \sin m\pi x,$$
$$\Theta_f = A_2 \sin n\pi y \cos m\pi x, \tag{A16}$$
$$\Theta_s = A_3 \sin n\pi y \cos m\pi x,$$

where m and n are the horizontal and vertical cell numbers, respectively. Inserting these expressions in the linearized governing equations yields

$$\begin{pmatrix} m^2\pi^2 + n^2\pi^2 & \text{Ra}^* m\pi & 0 \\ m\pi & \gamma(m^2\pi^2 + n^2\pi^2) + \mathcal{H} & \sigma(m^2\pi^2 + n^2\pi^2) - \mathcal{H} \\ 0 & \sigma\lambda(m^2\pi^2 + n^2\pi^2) - \mathcal{H}\lambda & \eta\lambda(m^2\pi^2 + n^2\pi^2) + \mathcal{H}\lambda \end{pmatrix} \times (A_1 A_2 A_3) = (000).$$

The critical Rayleigh number Ra* can then be found by setting the determinant of the matrix to zero:

$$\text{Ra}^* = \frac{\pi^2(m^2+n^2)^2}{m^2}\frac{[(m^2\pi^2 + n^2\pi^2)(\gamma\eta - \sigma^2) + \mathcal{H}(\gamma + \eta + 2\sigma)]}{[\eta(m^2\pi^2 + n^2\pi^2) + \mathcal{H}]}. \tag{A17}$$

Equation (A17) can now be used for analyzing both LTNE models at the onset of convection. By setting $\sigma = 0$, Eq. (A17) recovers the stability behavior of the LTNE-1 model. First, by temporarily setting k_m to be equal to the upper limit value, namely, $k_{m,\max} = \varphi k_f + (1-\varphi)k_s$, our analysis should recover the results from Banu and Rees [51]. This is shown in Fig. 12, where we observe that the critical Rayleigh number for the onset of convection is always lower than the classical $4\pi^2$ value for the whole range of normalized interphase heat transfer coefficient $\mathcal{H}$. The true stagnant thermal conductivity of the porous medium takes values lower than this upper limit, whose effect is to raise the critical Rayleigh number at the LTE limit, which has been shown

in Fig. 2(a). Comparing Figs. 12 and 2(a) shows the fact that correcting the value of the stagnant thermal conductivity from the upper limit value of $k_{m,\max}$ to the correct value k_m significantly changes the value of the critical Rayleigh number.

[1] D. A. Nield and A. Bejan, *Convection in Porous Media* (Springer-Verlag, New York, 2013).
[2] C. W. Horton and F. T. Rogers, J. Appl. Phys. **16** (1945).
[3] E. R. Lapwood, Math. Proc. Cambridge Philos. Soc. **44**, 508 (1948).
[4] P. Cheng, Adv. in Heat Transfer **14**, 1 (1979).
[5] T. Jonsson and I. Catton, J. Heat Transfer **109**, 371 (1987).
[6] N. Kladias and V. Prasad, J. Thermophys. Heat Transfer **5**, 560 (1991).
[7] S. Chen and G. D. Doolen, Annu. Rev. Fluid Mech. **30**, 329 (1998).
[8] C. K. Aidun and J. R. Clausen, Annu. Rev. Fluid Mech. **42**, 439 (2010).
[9] Y. Davit, C. G. Bell, H. M. Byrne, L. A. C. Chapman, L. S. Kimpton, G. E. Lang, K. H. L. Leonard, J. M. Oliver, N. C. Pearson, R. J. Shipley, S. L. Waters, J. P. Whiteley, B. D. Wood, and M. Quintard, Adv. Water Resour. **62**, 178 (2013).
[10] M. Quintard and S. Whitaker, Adv. Heat Transfer **23**, 369 (1993).
[11] M. Quintard, M. Kaviany, and S. Whitaker, Adv. Water Resour. **20**, 77 (1997).
[12] F. Kuwahara, M. Shirota, and A. Nakayama, Int. J. Heat Mass Transfer **44**, 1153 (2001).
[13] J. G. Fourie and J. P. Du Plessis, Transp. Porous Media **53**, 163 (2003).
[14] Y. H. Qian, D. D'Humires, and P. Lallemand, Europhys. Lett. **17**, 479 (1992).
[15] H. Karani and C. Huber, Phys. Rev. E **91**, 023304 (2015).
[16] L. Li, C. Chen, R. Mei, and J. F. Klausner, Phys. Rev. E **89**, 043308 (2014).
[17] H. Yoshida, T. Kobayashi, H. Hayashi, T. Kinjo, H. Washizu, and K. Fukuzawa, Phys. Rev. E **90**, 013303 (2014).
[18] R. Huang and H. Wu, J. Comput. Phys. **294**, 346 (2015).
[19] S. Chen, B. Yang, and C. Zheng, Int. J. Heat Mass Transfer **102**, 637 (2016).
[20] S. Chen, Y. Yan, and W. Gong, Int. J. Heat Mass Transfer **107**, 862 (2017).
[21] G. Pareschi, N. Frapolli, S. S. Chikatamarla, and I. V. Karlin, Phys. Rev. E **94**, 013305 (2016).
[22] Y. Hu, D. Li, S. Shu, and X. Niu, Phys. Rev. E **92**, 063305 (2015).
[23] Z. Hu, J. Huang, and W.-A. Yong, Phys. Rev. E **93**, 043320 (2016).
[24] D. Gao, Z. Chen, L. Chen, and D. Zhang, Int. J. Heat Mass Transfer **105**, 673 (2017).
[25] T. Inamuro, M. Yoshino, and F. Ogino, Phys. Fluids **7**, 2928 (1995).
[26] Q. Zou and X. He, Phys. Fluids **9**, 1591 (1997).
[27] A. D'Orazio and S. Succi, in *Computational Science ICCS 2003*, edited by P. M. Sloot, D. Abramson, A. Bogdanov, J. J. Dongarra, A. Y. Zomaya, and Y. E. Gorbachev, Lecture Notes in Computer Science Vol. 2657 (Springer, Berlin, 2003), pp. 977–986.
[28] A. D'Orazio, M. Corcione, and G. P. Celata, Int. J. Therm. Sci. **43**, 575 (2004).
[29] M. Wang and N. Pan, Mater. Sci. Eng.: R: Rep. **63**, 1 (2008).
[30] S. Torquato, *Random Heterogeneous Materials: Microstructure and Macroscopic Properties*, Interdisciplinary Applied Mathematics (Springer, New York, 2005).
[31] D. A. S. Rees and I. Pop, in *Transport Phenomena in Porous Media III*, edited by D. Ingham and I. Pop (Pergamon Press, Oxford, 2005), pp. 147–173.
[32] A. Nakayama, F. Kuwahara, M. Sugiyama, and G. Xu, Int. J. Heat Mass Transfer **44**, 4375 (2001).
[33] C. T. Hsu, J. Heat Transfer **121**, 733 (1999).
[34] S. Emmanuel and B. Berkowitz, Transp. Porous Media **67**, 413 (2007).
[35] D. A. S. Rees, A. P. Bassom, and P. G. Siddheshwar, J. Fluid Mech. **594**, 379 (2008).
[36] D. Henry, R. Touihri, R. Bouhlila, and H. Ben Hadid, Water Resour. Res. **48**, W10538 (2012).
[37] J. M. Straus, J. Fluid Mech. **64**, 51 (1974).
[38] J. Levec and R. G. Carbonell, AIChE J. **31**, 581 (1985).
[39] C. Hsu and P. Cheng, Int. J. Heat Mass Transfer **33**, 1587 (1990).
[40] G. Taylor, Proc. R. Soc. A **219**, 186 (1953).
[41] P. G. Saffman, J. Fluid Mech. **7**, 194 (1960).
[42] M. Poreh, J. Geophys. Res. **70**, 3909 (1965).
[43] J. G. Georgiadis and I. Catton, Phys. Fluids **30**, 1017 (1987).
[44] F. Kuwahara, A. Nakayama, and H. Koyama, J. Heat Transfer **118**, 756 (1996).
[45] M. H. Pedras and M. J. de Lemos, Int. J. Heat Mass Transfer **51**, 5359 (2008).
[46] N. Jeong and D. H. Choi, Int. J. Heat Mass Transfer **54**, 4389 (2011).
[47] H. Neischloss and G. Dagan, Phys. Fluids **18**, 757 (1975).
[48] O. Kvernvold and P. A. Tyvand, J. Fluid Mech. **99**, 673 (1980).
[49] C. R. B. Lister, J. Fluid Mech. **214**, 287 (1990).
[50] J. G. Georgiadis and I. Catton, Int. J. Heat Mass Transfer **31**, 1081 (1988).
[51] N. Banu and D. Rees, Int. J. Heat Mass Transfer **45**, 2221 (2002).